Control Engineering Practice 85 (2019) 235–245

Contents lists available at ScienceDirect

Control Engineering Practice

journal homepage: www.elsevier.com/locate/conengprac

Comparison of control design models and observers for dynamic positioning of surface vessels

Svenn A. Værnø [a,*], Roger Skjetne [a], Øivind K. Kjerstad [b], Vincenzo Calabrò [c]

[a] Department of Marine Technology, Norwegian University of Science and Technology, 7491 Trondheim, Norway
[b] University Centre in Svalbard, Norway
[c] Kongsberg Maritime AS, Norway

ARTICLE INFO

Keywords:
Dynamic positioning
Marine vessels
Observers
Modeling
Optimization

ABSTRACT

This paper investigates some fundamental aspects of control system design for dynamic positioning of marine surface vessels. Different control design models are compared. The impact of applying linear and nonlinear models to describe the hydrodynamic damping loads are investigated, and common observer algorithms for DP are compared. The comparison includes a linear time-varying Kalman filter, an extended Kalman filter, and an unscented Kalman filter. To make the comparisons rigorous, optimization is employed to find optimal observer gains, and high-fidelity simulation data and full-scale experimental data are used to test the performance under operations/conditions with significant transient effects.

1. Introduction

In a model-based control and observer design, the performance of the control and observer algorithms strongly depends on how well the underlying model captures the dynamics of the system. The modeling of marine surface vessels performing dynamic positioning (DP) has an extensive literature; see for instance Fossen (2011) and Sørensen (2011) where high-fidelity models are described in detail, along with different models for controller and model-based observer design. However, there are few rigorous comparisons of control design models in the literature. There are papers where observers and controllers based on control design models have been shown to work well, as for instance by Fossen and Strand (1999), and Tannuri and Morishita (2006), where experimental validations were presented. In the work by Refsnes and Sørensen (2007) two control design models were compared for a linear system subject to an ocean current. A similar study is done by Refsnes (2007) where different control design models were compared for autonomous underwater vehicles (AUV's) subject to ocean currents. The study reported by Refsnes (2007) used a number of injection gains for each observer. However, the simulation model used to simulate the plant dynamics matches one of the control design models, giving the observers based on this model a clear advantage in their simulation study.

There exist a number of papers where different observer algorithms are presented and tested for DP. Early work on using the Kalman filter for DP was presented by Grimble, Patton, and Wise (1980) and Fung and Grimble (1983), and the Extended Kalman Filter (EKF) by Balchen, Jenssen, and Sælid (1976) and Saelid, Jenssen, and Balchen (1983). In the work by Fossen and Strand (1999) the authors presented a nonlinear (passive) observer (NLO) with full-scale experimental results, and in Tannuri and Morishita (2006) experimental results of a typical DP system using an EKF was presented. However, to the authors' knowledge, there are no papers with a rigorous comparison of the different algorithms applied to DP. In Fossen and Strand (1999), the authors argued that the NLO has some benefits compared to the EKF. The NLO has fewer tuning parameters and is shown to be UGES, whereas there is no global stability guarantee for the EKF. In terms of performance, the EKF has time-varying gains initially, whereas the NLO is a fixed-gain observer. Additionally, the NLO assumes that the rotation matrix is a signal, using the measured heading angle, whereas the EKF uses the low-frequency (LF) heading as a state in the rotation matrix. Especially in moderate to high sea states, this EKF mechanism should be beneficial. In Candeloro, Sørensen, Longhi, and Dukan (2012) different observer algorithms were compared for remotely operated vehicles (ROVs), but the tuning of the observers is found in an ad hoc manner, so a definite conclusion on performance is difficult.

In this work a rigorous analysis of the performance of both the models and observer algorithms for DP is reported, using derivative-free optimization (DFO). Different model structures to capture the environmental loads and unmodeled dynamics are analyzed. This includes a comparison of using nonlinear damping as opposed to just linear damping. For each such model, different observer algorithms are then quantitatively compared using a high-fidelity simulation model of a

* Corresponding author.
E-mail addresses: svenn.are.varno@ntnu.no (S.A. Værnø), roger.skjetne@ntnu.no (R. Skjetne), oivind.kjerstad@unis.no (Ø.K. Kjerstad), v.calabro@ieee.org (V. Calabrò).

https://doi.org/10.1016/j.conengprac.2019.01.015
Received 8 May 2018; Received in revised form 24 January 2019; Accepted 24 January 2019
Available online 19 February 2019
0967-0661/

supply vessel and full-scale data from DP operations of R/V Gunnerus. The observers are an EKF, an Unscented Kalman Filter (UKF), and a Linear Time-Varying Kalman-Filter (LTV-KF). The natural comparison is to compare the EKF with the NLO, the two most applied DP observers. However, it is easier to rigorously compare Kalman filters, since they have the same structure and the DFO can optimize on the same parameters. The LTV-KF is the Kalman filter equivalent of the NLO, provided only linear damping is included. Typically when the NLO is implemented for DP in the literature (Fossen & Strand, 1999; Loria, Fossen, & Panteley, 2000), only the linear damping is included. Since the yaw angle is assumed to be a signal, the rotation matrix can be assumed to be a known time-varying matrix, and the system is linear time-varying. Thus, a linear Kalman filter can be applied. When the LTV-KF reaches steady state Kalman gains, the LTV-KF and the NLO are identical in structure.

The last observer algorithm that is included in the comparison is the UKF. This is a nonlinear filter that does not rely on linearized dynamics as the EKF, thus being interesting for the comparison. The UKF is better at handling nonlinearities than the EKF (Simon, 2006), and it also has the benefit of using the low-frequency heading angle as a state (and not a signal) in the rotation matrix.

The main contribution of this paper is a systematic comparison of residual load models and Kalman filter algorithms for DP of marine surface vessels, using derivative-free optimization on test data that holds significant transient effects. The effect of using nonlinear damping versus only linear damping is tested. Both high-fidelity simulation data and full-scale experimental data from the AMOS DP Cruise 2016 (Skjetne et al., 2017) are used.

Nomenclature

Notation

A column vector is stated as $\mathrm{col}\,(\boldsymbol{x},\boldsymbol{y},\boldsymbol{z}) := \left[\boldsymbol{x}^\top,\boldsymbol{y}^\top,\boldsymbol{z}^\top\right]^\top$, $\mathbb{R}_{>0}$ denotes positive real numbers, and $\mathbb{S}$ represents the angle defined on the interval $[-\pi,\pi)$.

Abbreviations

AUV Autonomous underwater vehicle

CDM Control design model

DFO Derivative free optimization

DOF Degrees of freedom

EKF Dynamic positioning

LF Low frequency

LTV-KF Linear time-varying Kalman filter

NED North-East-Down

NLO Nonlinear observer

SVM Simulation verification model

UGES Uniformly globally exponentially stable

UKF Unscented Kalman filter

2. Problem formulation

The two reference frames used in DP are the North-East-Down (NED) frame, which is a local Earth-fixed frame assumed inertial (with x-axis pointing North, y-axis pointing East, and z-axis pointing down), and the body-fixed frame, which typically has the origin in the waterline along the centerline of the vessel(with x-axis pointing in the direction of the bow, y-axis pointing starboard, and z pointing down).

In the following there is a distinction between the *simulation verification model (SVM)* and the *control design model* (CDM). The former is a higher fidelity model used for controller and observer verification, whereas the latter is used for observer and controller design. The CDM captures the main dynamics, and for DP this includes the part of the model relevant for low-speed maneuvers, that is, Coriolis and centripetal terms are often omitted, and typically the nonlinear damping effects as well (Fossen, 2011). A bias load model is then typically applied to capture the residual loads in the CDM. These are uncertainties related to ocean current loads, slowly-varying wave drift loads, differences between actual wind loads and the estimated wind loads from the wind sensor measurements, unmodeled dynamics in the thruster system, and parametric uncertainties in the mass/inertia and damping terms.

2.1. Overall control design model

The CDM used in this study is the 3 DOF model (Fossen, 2011; Fossen & Perez, 2009; Sørensen, 2011)

$$\dot{\boldsymbol{\xi}} = \boldsymbol{A}_{\boldsymbol{w}}\boldsymbol{\xi} + \boldsymbol{E}_{\boldsymbol{w}}\boldsymbol{w}_{\boldsymbol{w}} \tag{1a}$$

$$\dot{\boldsymbol{\eta}} = \boldsymbol{R}(\psi)\boldsymbol{\nu} \tag{1b}$$

$$\boldsymbol{M}\dot{\boldsymbol{\nu}} + \boldsymbol{d} = \boldsymbol{\tau} + \boldsymbol{w}_{\boldsymbol{\nu}} \tag{1c}$$

$$\boldsymbol{y} = \boldsymbol{\eta} + \boldsymbol{C}_{\boldsymbol{w}}\boldsymbol{\xi} + \boldsymbol{v}_{\boldsymbol{y}}, \tag{1d}$$

where $\boldsymbol{\xi} \in \mathbb{R}^6$ models the wave-frequency motion by a damped oscillation model. $\boldsymbol{A}_{\boldsymbol{w}}$ is a Hurwitz matrix that contains the damping ratio of the wave motion model and the peak frequency of the sea state, and $\boldsymbol{w}_{\boldsymbol{w}} \in \mathbb{R}^3$ is white noise; see Fossen (2011) for details. There is a separation between the wave-frequency motion in (1a) and the low-frequency motion of the vessel in (1b)–(1c). In low-speed applications such as DP, it is typically only interesting to control the low-frequency motion of the vessel, since compensating the first-order wave motion causes extra wear and tear on the thrusters, and in most cases it is not possible to compensate this motion. The vector $\boldsymbol{\eta} = \mathrm{col}\,(\eta_N,\eta_E,\psi) \in \mathbb{R}^2\times\mathbb{S}$ is the low-frequency North/East position and heading angle of the vessel, and $\boldsymbol{\nu} = \mathrm{col}\,(u,v,r) \in \mathbb{R}^3$ is the low-frequency surge/sway velocity in the body-frame, and the yaw rate, respectively. The matrix $\boldsymbol{R}(\psi)$ rotates a 3 DOF vector from body to NED according to

$$\boldsymbol{R}(\psi) = \begin{bmatrix} \cos(\psi) & -\sin(\psi) & 0 \\ \sin(\psi) & \cos(\psi) & 0 \\ 0 & 0 & 1 \end{bmatrix}. \tag{2}$$

The mass matrix contains the inertia and added mass parameters of the vessel, and $\boldsymbol{\tau} \in \mathbb{R}^3$ is the control vector formed by propulsion loads.

The measurement $\boldsymbol{y} \in \mathbb{R}^2\times\mathbb{S}$ is the sum of the low-frequency North/East position and heading vector η, the wave-frequency North/East position and heading vector $\boldsymbol{\eta}_{\boldsymbol{w}} = \boldsymbol{C}_{\boldsymbol{w}}\boldsymbol{\xi}$, where $\boldsymbol{C}_{\boldsymbol{w}} = \begin{bmatrix}\boldsymbol{0}_{3\times3} & \boldsymbol{I}_{3\times3}\end{bmatrix}$, and the measurement noise $\boldsymbol{v}_{\boldsymbol{y}} \in \mathbb{R}^3$.

Remark 1. It is assumed that only the vector $\boldsymbol{\eta}$ is measured through $\boldsymbol{y}$ in (1d). If, however, also the velocity $\boldsymbol{\nu}$ is accurately measured, for example through a measurement equation $\boldsymbol{y}_{\boldsymbol{\nu}} = \boldsymbol{R}(\boldsymbol{\psi})\boldsymbol{\nu} + \boldsymbol{C}_{\boldsymbol{w}}\boldsymbol{A}_{\boldsymbol{w}}\boldsymbol{\xi} + \boldsymbol{v}_{\boldsymbol{\nu}}$ from a sophisticated navigation system, then this can with ease be included in the measurement equations of the observer, typically resulting in improved estimation accuracy of the overall state vector.

The load vector $\boldsymbol{d} \in \mathbb{R}^3$ contains hydrodynamic damping loads, slowly-varying second order wave drift loads, and other unmodeled dynamics such as parametric uncertainties in the mass/inertia and damping terms, and errors in thrust modeling. Different choices for $\boldsymbol{d}$ are outlined in the next section.

2.2. Damping and bias load models

Control design models for DP can differ in their complexity, but they also differ in how the residual loads such as current, second order wave loads, and unmodeled dynamics are accounted for in the model. In the state estimator, using only GNSS and compass measurements, it is not possible to separate the different environmental loads and unmodeled dynamics, so they are lumped together and estimated as one bias load vector. The most common assumption is that these loads are slowly-varying (or even constant) in the NED-frame so that they can be compensated by a type of integral action. However, even if the environmental loads are constant in the NED-frame, they will not be constant as experienced by the vessel, due to vessel hull geometry. Another method is to model the unknowns as a current vector, which should be more accurate in terms of estimating environmental disturbances, such as current and second order wave loads. This model, contrary to the bias vector model, takes the vessel hull into account by including the damping matrix. In addition, if the current is irrotational and constant, this load is accurately described as a NED-fixed current. However, there are other loads that has to be accounted for as well. Errors in the damping parameters become a body-fixed bias load, and so do errors in the thrust modeling and mapping. Therefore, the choice of the most accurate model is not obvious.

Another motivation for model choice in the literature concerns the stability proofs of the observer and controller designs. These typically require an assumption on the external and unmodeled loads, either that they are constant in the NED- or the body-frame. Neither is 100% correct.

Next, the different models for $\boldsymbol{d}$ in (1c) are presented.

Residual load modeling. CDMs 1 and 2 capture the environment and unmodeled dynamics as a load vector assumed constant in the NED-frame and body-frame, respectively.

CDM 1 (NED-fixed):

$$\boldsymbol{d} := \boldsymbol{D}(\boldsymbol{\nu})\boldsymbol{\nu} - \boldsymbol{R}(\psi)^\top \boldsymbol{b}^n \tag{3a}$$

$$\dot{\boldsymbol{b}}^n = \boldsymbol{w}_b, \tag{3b}$$

where $\boldsymbol{b}^n \in \mathbb{R}^3$ is a NED-fixed bias load vector, $\boldsymbol{w}_b \in \mathbb{R}^3$ is white noise, and the damping matrix $\boldsymbol{D}(\boldsymbol{\nu})\boldsymbol{\nu}$ is given as

$$\boldsymbol{D}(\boldsymbol{\nu})\boldsymbol{\nu} := \boldsymbol{D}_L\boldsymbol{\nu} + \boldsymbol{D}_{NL}(\boldsymbol{\nu})\boldsymbol{\nu} \tag{4}$$

where $\boldsymbol{D}_L, \boldsymbol{D}_{NL}(\boldsymbol{\nu}) \in \mathbb{R}^{3\times 3}$ are the linear and nonlinear damping matrices, respectively. The bias model (3b) is the common random walk model used in the literature; see for instance Kjerstad and Skjetne (2016). Another common version of (3b) is the Markov model (Sørensen, 2011). However, typically the time constant is very large, essentially making it a random walk model as in (3b).

CDM 2 (body-fixed):

$$\boldsymbol{d} := \boldsymbol{D}(\boldsymbol{\nu})\boldsymbol{\nu} - \boldsymbol{b}^b \tag{5a}$$

$$\dot{\boldsymbol{b}}^b = \boldsymbol{w}_b, \tag{5b}$$

where $\boldsymbol{b}^b \in \mathbb{R}^3$ is a body-fixed bias load vector. Since unmodeled dynamics and other load effects often are body-fixed, it makes good sense to include the bias $\boldsymbol{b}$ as a body-fixed vector. In addition, this model is typically used in linearized models; see for instance Fossen and Perez (2009) and Hassani, Pascoal, Aguiar, et al. (2012).

Current estimation. CDMs 3 and 4 are current models with ocean currents assumed constant in the NED-frame and the body-frame, respectively.

CDM 3 (NED-fixed):

$$\boldsymbol{d} := \boldsymbol{D}(\boldsymbol{\nu}_r)\boldsymbol{\nu}_r \tag{6a}$$

$$\dot{\boldsymbol{\nu}}_c^n = \boldsymbol{w}_c \tag{6b}$$

$$\boldsymbol{\nu}_r = \boldsymbol{\nu} - \boldsymbol{R}(\psi)^\top \begin{bmatrix} \boldsymbol{\nu}_c^n \\ 0 \end{bmatrix}, \tag{6c}$$

where $\boldsymbol{\nu}_c^n \in \mathbb{R}^2$ is an unknown NED-fixed current vector, and $\boldsymbol{w}_c \in \mathbb{R}^2$ is white noise.

CDM 4 (body-fixed):

$$\boldsymbol{d} := \boldsymbol{D}(\boldsymbol{\nu}_r)\boldsymbol{\nu}_r \tag{7a}$$

$$\dot{\boldsymbol{\nu}}_c^b = \boldsymbol{w}_c \tag{7b}$$

$$\boldsymbol{\nu}_r = \boldsymbol{\nu} - \begin{bmatrix} \boldsymbol{\nu}_c^b \\ 0 \end{bmatrix}, \tag{7c}$$

$\boldsymbol{\nu}_c^b \in \mathbb{R}^2$ is an unknown body-fixed current vector.

The different CDMs are summarized in Table 1.

Table 1
The control design models.

CDM	Description
1	Bias load model, NED-fixed
2	Bias load model, body-fixed
3	Current model, NED-fixed
4	Current model, body-fixed

2.3. Observer realizations

For all implementations, the models are discretized and discrete-time observers are used. The following continuous dynamics covers all models in this paper,

$$\dot{\boldsymbol{x}} = \boldsymbol{A}(t,\boldsymbol{x})\boldsymbol{x} + \boldsymbol{B}\boldsymbol{u} + \boldsymbol{E}\boldsymbol{w} \tag{8a}$$

$$\boldsymbol{y} = \boldsymbol{C}\boldsymbol{x} + \boldsymbol{v}, \tag{8b}$$

and the discretized system becomes

$$\begin{aligned} \boldsymbol{x}_k &= \boldsymbol{f}_{k-1}(\boldsymbol{x}_{k-1}, t_{k-1}, \boldsymbol{u}_{k-1}, \boldsymbol{w}_{k-1}) && (9a)\\ &= \boldsymbol{\Phi}_{k-1}(\boldsymbol{x}_{k-1}, t_{k-1})\boldsymbol{x}_{k-1} + \boldsymbol{\Delta}_{k-1}(\boldsymbol{x}_{k-1}, t_{k-1})\boldsymbol{u}_{k-1} \\ &\quad + \boldsymbol{\Gamma}_{k-1}(\boldsymbol{x}_{k-1}, t_{k-1})\boldsymbol{w}_{k-1} && (9b)\end{aligned}$$

$$\boldsymbol{y}_k = \boldsymbol{H}_k\boldsymbol{x}_k + \boldsymbol{v}_k \tag{9c}$$

$$\boldsymbol{w}_k \sim (\boldsymbol{0}, \boldsymbol{Q}_k) \tag{9d}$$

$$\boldsymbol{v}_k \sim (\boldsymbol{0}, \boldsymbol{R}_k), \tag{9e}$$

where, using Taylor expansion (Chen, 2009; Fossen, 2011) and sampling time $h = 0.1$ s gives

$$\boldsymbol{\Phi}_k = \mathrm{e}^{\boldsymbol{A}(t_k,\boldsymbol{x}_k)h} \approx \boldsymbol{I} + \boldsymbol{A}(t_k,\boldsymbol{x}_k)h + \frac{1}{2}(\boldsymbol{A}(t_k,\boldsymbol{x}_k)h)^2 \tag{10a}$$

$$\boldsymbol{\Delta}_k = \left(\int_0^h \mathrm{e}^{\boldsymbol{A}h}d\sigma\right)\boldsymbol{B} \approx \left(\boldsymbol{I}h + \frac{1}{2}\boldsymbol{A}(t_k,\boldsymbol{x}_k)h^2 + \frac{1}{6}\boldsymbol{A}(t_k,\boldsymbol{x}_k)^2h^3\right)\boldsymbol{B} \tag{10b}$$

$$\boldsymbol{\Gamma}_k = \left(\int_0^h \mathrm{e}^{\boldsymbol{A}(t_k,\boldsymbol{x}_k)h}d\sigma\right)\boldsymbol{E} \approx \left(\boldsymbol{I}h + \frac{1}{2}\boldsymbol{A}(t_k,\boldsymbol{x}_k)h^2 + \frac{1}{6}\boldsymbol{A}(t_k,\boldsymbol{x}_k)^2h^3\right)\boldsymbol{E} \tag{10c}$$

$$\boldsymbol{H}_k = \boldsymbol{C}. \tag{10d}$$

The goal is not to obtain the best and most accurate observer, but to have a fair comparison between the models and observers being investigated. Because of this, the sample time is set quite high to keep the run-time of the DFOs low.

Kalman filters

The Kalman filters have been implemented as in Simon (2006). The implementation for the LTV-KF and the EKF are given below, and the UKF implementation is shown in Appendix A.

- Initialization:

$$\hat{\boldsymbol{x}}_0^+ = E(\boldsymbol{x}_0) \tag{11a}$$

$$\boldsymbol{P}_{\boldsymbol{0}}^+ = E[(\boldsymbol{x}_0 - \hat{\boldsymbol{x}}_0^+)(\boldsymbol{x}_{\boldsymbol{0}} - \hat{\boldsymbol{x}}_0^+)^\top] \tag{11b}$$

- Kalman Filter equations LTV-KF and EKF (Simon, 2006):

$$\boldsymbol{P}_{\boldsymbol{k}}^- = \boldsymbol{F}_{\boldsymbol{k-1}}\boldsymbol{P}_{\boldsymbol{k-1}}^+\boldsymbol{F}_{\boldsymbol{k-1}}^\top + \boldsymbol{\Gamma}_{\boldsymbol{k-1}}\boldsymbol{Q}_{\boldsymbol{k-1}}\boldsymbol{\Gamma}_{\boldsymbol{k-1}}^\top \tag{12a}$$

$$\boldsymbol{K}_{\boldsymbol{k}} = \boldsymbol{P}_{\boldsymbol{k}}^-\boldsymbol{H}_{\boldsymbol{k}}^\top(\boldsymbol{H}_{\boldsymbol{k}}\boldsymbol{P}_{\boldsymbol{k}}^-\boldsymbol{H}_{\boldsymbol{k}}^\top + \boldsymbol{R}_{\boldsymbol{k}})^{-1} \tag{12b}$$

$$\hat{\boldsymbol{x}}_{\boldsymbol{k}}^- = \boldsymbol{\Phi}_{\boldsymbol{k-1}}(t_{k-1})\hat{\boldsymbol{x}}_{\boldsymbol{k}}^+ + \boldsymbol{\Delta}_{\boldsymbol{k-1}}(t_{k-1})\boldsymbol{u}_{\boldsymbol{k-1}} \quad \text{(LTV-KF)} \tag{12c}$$

$$\hat{\boldsymbol{x}}_{\boldsymbol{k}}^- = \boldsymbol{f}_{\boldsymbol{k-1}}(\hat{\boldsymbol{x}}_{\boldsymbol{k-1}}^+, \boldsymbol{u}_{\boldsymbol{k-1}}) \quad \text{(EKF)} \tag{12d}$$

$$\hat{\boldsymbol{x}}_{\boldsymbol{k}^+} = \hat{\boldsymbol{x}}_{\boldsymbol{k}}^- + \boldsymbol{K}_k(\boldsymbol{y}(k) - \boldsymbol{H}_{\boldsymbol{k}}\hat{\boldsymbol{x}}_{\boldsymbol{k}}^-) \tag{12e}$$

$$\boldsymbol{P}_{\boldsymbol{k}}^+ = (\boldsymbol{I} - \boldsymbol{K}_{\boldsymbol{k}}\boldsymbol{H}_{\boldsymbol{k}})\boldsymbol{P}_{\boldsymbol{k}}^-(\boldsymbol{I} - \boldsymbol{K}_{\boldsymbol{k}}\boldsymbol{H}_{\boldsymbol{k}})^\top + \boldsymbol{K}_{\boldsymbol{k}}\boldsymbol{R}_{\boldsymbol{k}}\boldsymbol{K}_{\boldsymbol{k}}^\top \tag{12f}$$

where $\boldsymbol{F}_{\boldsymbol{k}}$ is

$$\boldsymbol{F}_{k-1} = \boldsymbol{\Phi}_k(t_{k-1}) = \boldsymbol{\Phi}_{k-1}(\boldsymbol{\psi}_{k-1}^{\boldsymbol{m}}) \quad \text{(LTV-KF)}$$

$$\boldsymbol{F}_{k-1} = \frac{\partial \boldsymbol{f}_{k-1}}{\partial \boldsymbol{x}}\Big|_{\hat{\boldsymbol{x}}_{k-1}^+} \quad \text{(EKF)},$$

and $\boldsymbol{\psi}_{\boldsymbol{k}}^{\boldsymbol{m}}$ is the measured yaw angle at time step k.

2.4. Feedback control law

The controller $\boldsymbol{\tau}$ in (1c) has a feedforward and feedback component,

$$\boldsymbol{\tau} = \boldsymbol{\tau}_{FF} + \boldsymbol{\tau}_{FB}, \tag{13a}$$

where $\boldsymbol{\tau}_{FF}$ helps track the reference trajectory, and τ_{FB} is a PID (proportional–integral–derivative) tracking controller using state feedback,

$$\boldsymbol{\tau}_{FF} = \boldsymbol{D}\boldsymbol{\nu}_d(t) + \boldsymbol{M}\dot{\boldsymbol{\nu}}_d(t) \tag{13b}$$

$$\boldsymbol{\tau}_{FB} = -\boldsymbol{K}_{\boldsymbol{p}}\boldsymbol{R}(\psi)^\top(\hat{\boldsymbol{\eta}} - \boldsymbol{\eta}_d(t)) - \boldsymbol{K}_{\boldsymbol{d}}(\hat{\boldsymbol{\nu}} - \boldsymbol{\nu}_d(t)) - \boldsymbol{K}_{\boldsymbol{i}}\boldsymbol{R}(\psi)^\top\boldsymbol{\zeta} \tag{13c}$$

$$\dot{\boldsymbol{\zeta}} = \hat{\boldsymbol{\eta}} - \boldsymbol{\eta}_{\boldsymbol{d}}(t), \tag{13d}$$

where $\boldsymbol{\eta}_{\boldsymbol{d}}$, $\boldsymbol{\nu}_{\boldsymbol{d}}$, and $\dot{\boldsymbol{\nu}}_{\boldsymbol{d}(t)}$ are references generated by a guidance system and $\boldsymbol{K}_{\boldsymbol{p}}$, $\boldsymbol{K}_{\boldsymbol{d}}$ and $\boldsymbol{K}_{\boldsymbol{i}}$ are positive definite gain matrices, and $\hat{\boldsymbol{\eta}}$, $\hat{\boldsymbol{\nu}}$ are state estimates; for details see Sørensen (2013).

Remark 2. In a DP control law, the states $\hat{\boldsymbol{\eta}}$ and $\hat{\boldsymbol{\nu}}$ in (13) will be state estimates from the DP observer used in the loop. To generate the simulated dataset in this work, the LF state estimates $\hat{\boldsymbol{\eta}}$, $\hat{\boldsymbol{\nu}}$ from one well-tuned observer were used in the control law to track the reference trajectories. The different observers will then be tested and evaluated on this dataset. For the experimental data, the control input was given and the corresponding dataset will be used directly after some post-processing.

2.5. Derivative free optimization for comparison

To compare performance in the model and the observer investigation, optimization is used. A classic gradient decent-like method is not applicable, since information about the gradient, Hessian, or higher order derivatives are not available. Therefore, DFO is used.

The cost function used for the DFO in the paper is

$$J(\tilde{\boldsymbol{\eta}}, \tilde{\boldsymbol{\nu}}) = J_\eta(\tilde{\boldsymbol{\eta}}) + c_\nu J_\nu(\tilde{\boldsymbol{\nu}}) \tag{14a}$$

where

$$J_\eta(\tilde{\boldsymbol{\eta}}) = \sum_{k=0}^{n}(|\eta_{N,k} - \hat{\eta}_{N,k}| + |\eta_{E,k} - \hat{\eta}_{E,k}| + \frac{180}{\pi}|\psi_k - \hat{\psi}_k|) \tag{14b}$$

$$J_\nu(\tilde{\boldsymbol{\nu}}) = \sum_{k=0}^{n}(|u_k - \hat{u}_k| + |v_k - \hat{v}_k| + \frac{180}{\pi}|r_k - \hat{r}_k|). \tag{14c}$$

Here, $\tilde{\boldsymbol{\eta}} = \boldsymbol{\eta} - \boldsymbol{\eta}_d$, $\tilde{\boldsymbol{\nu}} = \boldsymbol{\nu} - \boldsymbol{\nu}_d$, $k = n$ is the final time step of the interval, and $c_\nu \in \mathbb{R}_{>0}$ is a scaling constant to weight the respective contributions from the estimation error in position and velocity. This scaling function is found iteratively and set such that the size of (14b) and (14c) are similar. Typical operating limits for DP is 3 m and 3 degrees (Veritas, 2011). The weighting in (14) is chosen to be close to this. In (14b), the cost on 1 m position error is chosen to be equivalent to 1 deg in heading. Similarly, 1 m/s error in linear velocity is equivalent to 1 deg/s angular velocity in (14c).

For a given dataset of n state, input, and output values according to the model (1), let $\mathcal{Y} = \{\boldsymbol{y}_0, \boldsymbol{y}_1, \boldsymbol{y}_2, \dots, \boldsymbol{y}_n\}$ be the set of measurement data according to (1d), $\mathcal{U} = \{\boldsymbol{u}_0, \boldsymbol{u}_1, \boldsymbol{u}_2, \dots, \boldsymbol{u}_n\}$ be the set of control input data according to (13), $\mathcal{H} = \{\boldsymbol{\eta}_0, \boldsymbol{\eta}_1, \boldsymbol{\eta}_2, \dots, \boldsymbol{\eta}_n\}$ be the set of low-frequency position/heading data according to (1b), and $\mathcal{V} = \{\boldsymbol{\nu}_0, \boldsymbol{\nu}_1, \boldsymbol{\nu}_2, \dots, \boldsymbol{\nu}_n\}$ be the set of low-frequency velocity data according to (1c). Let the selected observer algorithm be represented by the overall difference equation

$$\hat{\boldsymbol{X}}_k = \Gamma_{k-1}(\hat{\boldsymbol{X}}_{k-1}, \boldsymbol{u}_{k-1}, \boldsymbol{y}_k, \boldsymbol{K}) \tag{15}$$

where $\hat{\boldsymbol{X}}$ collects the overall state vector of the observer, and $\boldsymbol{K}$ represent the tunable observer gain vector. The optimization problem can then be formulated as

$$\underset{\boldsymbol{K}}{\text{minimize}} \qquad J(\tilde{\boldsymbol{\eta}}, \tilde{\boldsymbol{\nu}}) \tag{16a}$$

$$\text{subject to} \qquad \boldsymbol{y}_k \in \mathcal{Y}, \boldsymbol{u}_k \in \mathcal{U}, \boldsymbol{\eta}_k \in \mathcal{H}, \boldsymbol{\nu}_k \in \mathcal{V}, \text{ and (15)} \tag{16b}$$

with $J(\tilde{\boldsymbol{\eta}}, \tilde{\boldsymbol{\nu}})$ according to (14). Derivative-free optimization is then used to solve this optimization problem. For the high-fidelity simulation data, the data to evaluate the cost function are directly available from the simulation data. For the full-scale experimental data, on the other hand, the values used to evaluate the cost function (14) are the post-processed position/heading data, and from this the actual velocities are found by differentiating the resulting position/heading using a finite impulse response (FIR) filter.

2.6. Assumptions

For the linear LTV-KF, the heading angle in the rotation matrix is a measured signal. Thus $t \mapsto R(\psi(t)))$ is seen as a measured time-varying signal $\hat{R}(t)$. The assumption according to Fossen and Strand (1999) is made:

(A1) $R(\psi + \psi_w) \approx R(\psi)$; that is, the heading angle due to wave-induced motion, ψ_w, is negligible, since the wave-induced heading angle is typically less than 1° for normal sea states and less than 5° for extreme sea states (Price & Bishop, 1974),

and by (A1), the matrix signal $\hat{R}(t)$ approximates the low-frequency rotation matrix, $R(\psi)$.

2.7. Problem objective

The objective is to quantitatively compare the performance of the LTV-KF, EKF, and UKF observer algorithms over the four different residual load models (CDM1–CDM4) on several realistic (simulated and experimental) datasets containing transient operating and environmental conditions. Additionally, the effect of including nonlinear damping on the observer performance shall be particularly analyzed. The intended outcome is to gain deeper insight on the differences in performance for the investigated observers and models.

3. Setup

3.1. DP simulation verification model

The SVM is a 6 DOF high-fidelity model of a platform supply vessel with the main parameters listed in Table 2. The model includes waves, Coriolis, centripetal loads, linear damping, and nonlinear damping. The benefit of this model is the use of lookup tables for environmental forces, creating realistic variations of the environmental loads with

Table 2
Simulation, platform supply vessel, main parameters.

Parameters	Value
Length between perp.	80 m
Breadth	17.4 m
Draft	5.6 m
Displacement	6150 tons

Table 3
R/V Gunnerus, main parameters.

Parameters	Value
Length over all	31.3 m
Length between perp.	28.9 m
Breadth middle	9.6 m
Draft	2.7 m
Dead weight	107 tons

vessel heading, allowing for a fair comparison of the different control design models. The sea state has a significant wave height of 6 m, with a peak frequency of 0.53 rad/s taken from the JONSWAP[1] spectrum. The mean incident wave heading is 190° (head waves) in the North/East frame (Price & Bishop, 1974). The current has an initial velocity of 0.5 m/s and direction of 160° (bow). The SVM has realistic noise on the sensors, and the measurements are discretely updated at 1 Hz for the GPS and 10 Hz for the compass. The control action is implemented in discrete time with an update rate of 1 Hz. In addition, a first order filter (with time constant 5 s) is included to account for the actuator dynamics.

For the SVM, the linear damping is known from the model. The nonlinear damping was identified through several maneuvers with no waves or current. Maneuvers with pure surge, pure sway, and pure yaw were used to find the diagonal terms, and a maneuver with coupled sway and yaw motion was then used to find the cross-terms. The damping was identified also using DFO as described in Section 2.5. For details about the mass and damping parameters for the SVM, see Appendix B.

3.2. AMOS DP research cruise 2016

R/V Gunnerus is a 31 m long NTNU-owned research vessel, shown in Fig. 1, with main parameters in Table 3. Experimental full-scale data of R/V Gunnerus was collected during the AMOS DP Research Cruise (ADPRC) 2016. Kongsberg Maritime made available a test interface in the onboard commercial DP system, for the NTNU researchers to test different control and observer algorithms in real time and to log all necessary data during the trials (Skjetne et al., 2017).

On the sea trials for ADPRC, the DP 4-corner maneuver shown in Fig. 2 was performed. The waves were negligible, but there were current and wind during the sea trials. Three datasets are used, where dataset 1 had a current of velocity 0.6 m/s with direction 170°, and wind velocity of 5 m/s and direction 150°. Datasets 2 and 3 had similar environmental conditions, with a current of velocity 0.3 m/s with direction 300°, and wind velocity of 6 m/s and direction 250°.

The damping identification for the experimental data followed almost the same procedure as described for the SVM in Section 3.1, except for the identification of the linear damping matrix. For the simulation model, the linear damping matrix was known from the model. However, for the experimental data, the linear damping matrix was first identified as a standalone linear damping matrix, that is, for the case where only linear damping was used in the observer. For the identification of the nonlinear damping, the linear damping matrix as identified above was fixed and the model was further fit to the nonlinear terms. Thus, the same linear damping matrix is used when nonlinear damping is included. This makes the experimental data case similar to that of the simulation data case study. For details about the mass and damping parameters for R/V Gunnerus, see Appendix C.

[1] Joint North Sea Wave Project.

3.3. Application of the DFO

The MATLAB® function *fminsearch* has been adopted to run the DFO optimization according to (16). The DFO searches the points around the current value of the tunable observer gain $\boldsymbol{K}$ to see if any values give a lower cost for $J(\tilde{\boldsymbol{\eta}}, \tilde{\boldsymbol{\nu}})$. However, the DFO does only provide a local minimum, so it is therefore important to run simulations with several different initial conditions.

When DFO is used to find the optimal tuning for the Kalman filters, the Q-matrices (process noise) are restricted to be diagonal, and so is the initial covariance matrix. The constraint that the Kalman filters must start with a diagonal covariance matrix is not optimal for performance, but is in practice necessary for finding the minimum of the DFO cost function within a reasonable time. If all non-diagonal terms are to be included in the DFO, the problem becomes too large to solve, especially since several initial conditions have to be tested.

3.4. DP test cases

Two test cases of different characteristics are used to compare the models and observers, as described next.

Dp 4-corner test

The maneuver here called *DP 4-corner* is a box maneuver as shown in Fig. 2, where the vessel starts at $\boldsymbol{\eta} = \mathrm{col}(0m, 0m, 0°)$ with the following setpoint changes:

1. $\boldsymbol{\eta} = \mathrm{col}(40\mathrm{m}, 0m, 0°)$ (pure surge motion)
2. $\boldsymbol{\eta} = \mathrm{col}(40m, -40m, 0°)$ (pure sway motion)
3. $\boldsymbol{\eta} = \mathrm{col}(40m, -40m, -45°)$ (pure rotation)
4. $\boldsymbol{\eta} = \mathrm{col}(0m, -40m, -45°)$ (coupled surge/sway)
5. $\boldsymbol{\eta} = \mathrm{col}(0m, 0m, 0°)$ (coupled, all DOFs)

For each setpoint change above, the vessel follows a reference filter trajectory.

Transient test

Especially when comparing the control design models, a lot of transients are beneficial to trigger the potential differences in the models. The vessel is exposed to current and waves, and there is a setpoint change in both North/East and heading, that is, a coupled maneuver with a transient due to the heading change. For the setpoint change, the vessel follows a reference filter trajectory. Shortly thereafter there is a current direction change of 60°, and a slight change in current velocity, to simulate an unknown transient event. These changes are filtered through a first order filter with time constant of 30 s. The time frame between the two transients is short, which is deliberate to have three transient bias events (including initialization) in a short maneuver. The reference filter trajectories are shown in Fig. 3. Note that the reference trajectories are intentionally made fast compared to the size of the vessel (as seen in Table 2).

4. Results and discussion

Three different Kalman filters are compared; LTV-KF, EKF, and UKF for the four different control design models presented in Section 2.2. In addition, results for including nonlinear damping versus only linear damping are shown for the EKF and UKF. Results from the simulation cases as well as the experimental data are presented, before overall conclusions on the different observers and models are provided.

The tuning of the observers was found through DFO. First, several initial conditions was used to find minimum tuning of the LTV-KF algorithm. Then, variations around the minimum tuning for the LTV-KF was used as initial conditions to search for the minimum tuning of the EKF and the UKF.

Fig. 1. The R/V Gunnerus. Photo: Helge Sunde/Samfoto.

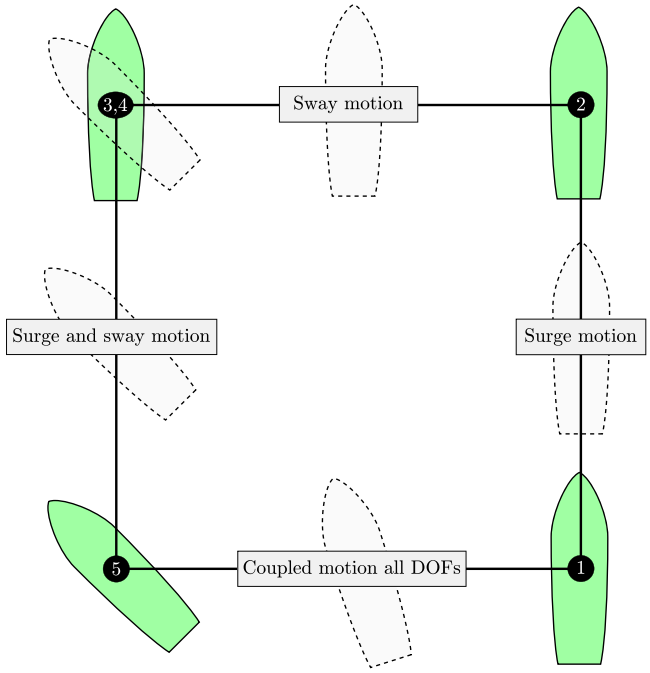

Fig. 2. The 4-corner DP test.

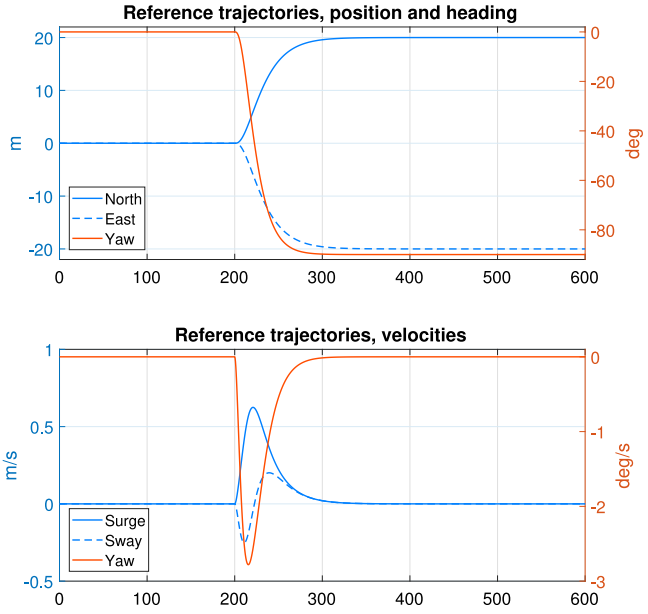

Fig. 3. Reference trajectories for the transient dataset.

4.1. Simulation results

For the simulation results, the high-fidelity model described in Section 3.1 was used with the transient dataset and the DP 4-corner dataset described in Section 3.4. At the beginning of the simulation, the position $\boldsymbol{\eta}$ and all observer states were initialized at zero, except the observer states for $\boldsymbol{\eta}_w$ from (1d) that was initialized at the measured position. The scaling factor in (14) was $c_v = 7$ for the simulation runs. The tuning was optimized for the transient dataset, and the same tuning was used for the DP 4-corner dataset. The environmental conditions in the two maneuvers were the same. Thus, by applying the tuning found through DFO for the transient dataset, the results for the DP 4-corner reveal how applicable the tuning was across the different maneuvers.

The results for the transient dataset are shown in Table 4 where the cost function $J(\tilde{\boldsymbol{\eta}}, \tilde{\boldsymbol{\nu}})$ from (14) is given for all the different combinations, and the results are normalized such that the worst performing $J(\tilde{\boldsymbol{\eta}}, \tilde{\boldsymbol{\nu}})$ has a score of 100. Fig. 4 shows time plots of how the cost function $J(\tilde{\boldsymbol{\eta}}, \tilde{\boldsymbol{\nu}})$ evolves for some of the CDM/observer combinations from Table 4. The plots show the best performing combination; the EKF using CDM 3 and nonlinear damping included, against the worst performing; the EKF using CDM 4 with only linear damping. Finally, the best performing LTV-KF version is plotted (using CDM 1). Note that the deviations mainly occur at the transients, that is, in the beginning, at 200 s, and at 400 s; see Section 3.4 for details about the transients.

From the results of the transient dataset, it is observed that the differences between the performance of the Kalman filters are small. The nonlinear damping significantly improves performance for CDMs 3 and 4, but only slightly for the CDMs 1 and 2. The differences between the CDMs are notable, but not significant.

The results for the DP 4-corner dataset are shown in Table 5, where it is observed that the differences between the observer algorithms are small also here. It is noted that the benefit of nonlinear damping is not as explicit as for the transient dataset. This is especially notable for CDMs 3 and 4. The differences between the four CDMs are smaller than for the transient dataset, and the best performing CDMs are different for the two datasets. That is true also when just linear damping is included.

For both the transient dataset and the DP 4-corner, the LTV-KF performs similarly to the EKF and UKF that use linear damping. In other words, there is no significant performance deterioration by using the measured yaw angle in the rotation matrix as a signal.

Table 4
Results on high fidelity simulation data: The transient dataset. The table shows the cost (14), where the results are normalized such that the worst performing J has a score of 100.

	EKF	UKF	LTV-KF	EKF(Lin.)	UKF(Lin.)
CDM 1	88.2	88.1	90.1	90.1	90.1
CDM 2	90.2	90.2	91.9	92.0	92.0
CDM 3	83.4	83.5	94.8	94.8	95.8
CDM 4	87.5	87.5	99.2	100.	100.

Table 5
Results on high fidelity simulation data: DP 4-corner dataset using the optimal tuning for the transient dataset. The table shows the cost (14), where the results are normalized such that the worst performing J has a score of 100.

	EKF	UKF	LTV-KF	EKF(Lin.)	UKF(Lin.)
CDM 1	94.9	94.9	97.0	96.9	96.9
CDM 2	100.	100.	98.0	98.0	98.0
CDM 3	91.8	91.8	92.4	92.4	92.4
CDM 4	90.5	90.5	91.9	92.0	92.0

4.2. Results from sea trials

The sea trial results are given for the three datasets described in Section 3.2, with the DP 4-corner test described in Section 3.4. The scaling factor in (14) was $c_v = 1.1$ for the experimental results. The resulting maneuver for dataset 1 is shown in Fig. 5. The tuning is optimized for dataset 1, and that tuning is thereafter applied for dataset 2 and dataset 3. This is to verify how well the tuning performs for maneuvers with different environmental conditions. Datasets 2 and 3 are performed in similar environmental conditions. The results are shown in Tables 6–8 for datasets 1, 2, and 3, respectively. The tables show the cost function $J(\tilde{\eta}, \tilde{\nu})$ from (14) where the results are normalized such that the worst performing J has a score of 100.

As found on the simulation data, the experimental results show that with the same CDM and damping matrix, the KFs have similar performance. This is a surprising results, especially considering that the UKF should be better at handling nonlinearities than the EKF. However, this indicates that the DP process is dominantly linear, and that using the measured heading angle in the rotation matrix may be sufficient. The three datasets did, however, contain a limited amount of environmental disturbances, since the weather conditions for the sea trials were very nice, and in such conditions the linear dynamics is even more dominant. However, dataset 1 does reveal a performance improvement using nonlinear damping. Note that the environmental conditions are similar for datasets 2 and 3.

CDMs 3 and 4 are good only if the EKF or UKF with nonlinear damping is used. Then a performance improvement over just using linear damping is observed. If linear damping (and bias) is used in the KFs, then the data supports using CDMs 1 or 2 (see Table 7).

4.3. Overall conclusions

The performance of the CDMs conclude somewhat differently for the high-fidelity simulation data versus the R/V Gunnerus full-scale data.

- For the simulation data, the EKF and UKF including nonlinear damping with CDM 3 perform the best for the transient dataset. The EKF and UKF including nonlinear damping with CDMs 3 and 4 perform the best for the 4-corner dataset.
- For the full-scale experimental datasets, CDM 1 performs the best. The performance is only slightly better for the EKF and UKF including nonlinear damping than the KFs with linear damping.
- If only using linear damping is considered for the simulation data, then the bias models (CDMs 1 and 2) perform best for the transient dataset, while the current models CDMs 3 and 4 are better for the 4-corner dataset.
- Including nonlinear damping gives a positive effect for the current models (CDMs 3 and 4), both for the simulation and experimental results. For the bias load models (CDM 1 and 2) the effect is negligible, and even slightly negative for CDM 2 on the 4-corner dataset on the simulation data.

Table 6
Experimental results for dataset 1. The table shows the cost (14), where the results are normalized such that the worst performing J has a score of 100.

	EKF	UKF	LTV-KF	EKF(Lin.)	UKF(Lin.)
CDM 1	90.8	90.8	91.1	91.0	91.0
CDM 2	91.9	91.9	92.2	92.2	92.2
CDM 3	93.2	93.2	100.	100.	100.
CDM 4	94.6	96.0	99.3	99.3	99.3

Table 7
Experimental results for dataset 2 using the optimal tuning for dataset 1. The table shows the cost (14), where the results are normalized such that the worst performing J has a score of 100.

	EKF	UKF	LTV-KF	EKF(Lin.)	UKF(Lin.)
CDM 1	97.5	97.4	97.5	97.5	97.5
CDM 2	99.0	99.0	99.0	99.0	99.0
CDM 3	96.9	96.9	100.	100.	100.
CDM 4	96.8	97.5	99.1	99.1	99.1

Table 8
Experimental results for dataset 3 using the optimal tuning for dataset 1. The table shows the cost (14), where the results are normalized such that the worst performing J has a score of 100.

	EKF	UKF	LTV-KF	EKF(Lin.)	UKF(Lin.)
CDM 1	96.4	96.4	96.8	96.8	96.8
CDM 2	97.0	97.0	97.4	97.4	97.4
CDM 3	97.6	97.6	100.	100.	100.
CDM 4	97.1	97.5	99.4	99.3	99.3

- In all test cases, the best performance is obtained by the EKF and/or UKF with nonlinear damping.

The fact that the current models perform better for the simulation data can be explained by richer environmental disturbances in the simulation, less uncertain and unmodeled dynamics, and vice versa for the experimental full-scale data.

Both the simulation and experimental data show that the different Kalman filters all performed similarly, showing that DP is dominantly a

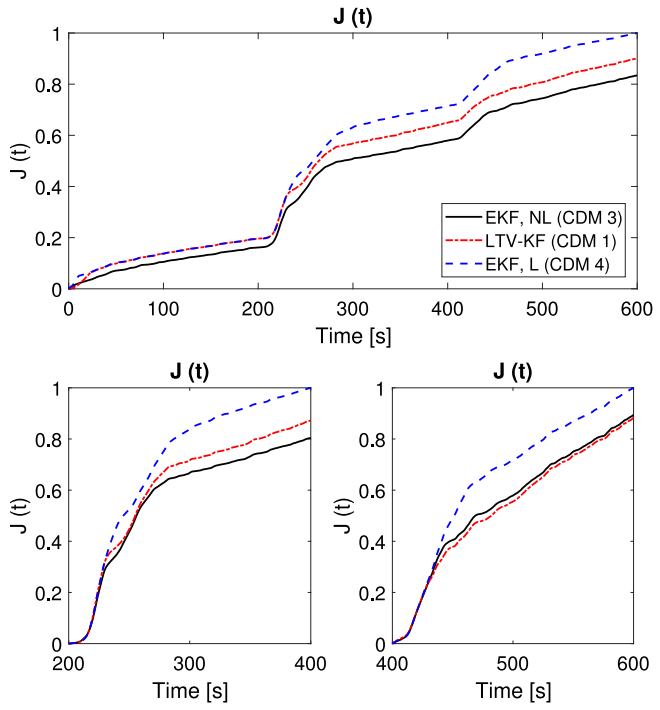

Fig. 4. Results from the simulation data using the transient dataset: The figures show the cost (14), where the results are normalized such that the worst performing J has a score of 1. In the figures, three of the combinations of observer algorithm and CDMs are shown. These are the EKF with CDM 3 and nonlinear damping (the best performing), the EKF with CDM 4 and linear damping (the worst performing), and the best performing version of the LTV-KF, that is, with CDM 1. The lower left plot starts at the setpoint change transient, and the lower right plot starts at the current direction transient; see Section 3.4 for details..

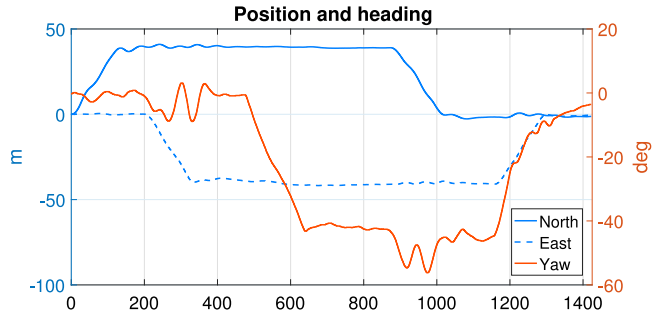

Fig. 5. Resulting position and heading for the experimental DP 4-corner test for dataset 1.

linear process. The nonlinear damping, however, gives a slight performance improvement. Both the simulation and experimental results show no significant performance deterioration when using the measured yaw angle in the rotation matrix with the LTV-KF instead of using the state estimate with the EKF/UKF. The LTV-KF performs similarly to the EKF and UKF when these use only linear damping.

Further work should put emphasis on the damping identification, especially for the experimental data. This could to a greater extent reveal what is achievable for the different control design models.

5. Conclusion

In this study different control design models and common Kalman filter algorithms for DP were compared for a high-fidelity simulation verification model of a supply vessel and for full-scale data from sea trials by R/V Gunnerus. In particular, the effect of including nonlinear damping in the observers was tested. The observer algorithms tested were the Linear Time-Varying Kalman Filter, the Extended Kalman Filter, and the Unscented Kalman Filter. The latter two were tested on both a linear damping model and a nonlinear damping model. The high-fidelity simulation data included waves, whereas the full-scale experimental data did not. The results indicated similar performance across the different design models and observers. The results justified that the DP process is dominantly linear, whereas a slight performance improvement can be obtained by using nonlinear damping (and consequently the EKF or UKF algorithms). However, the data from all the test cases did not show a clear indication of when to use the bias models, CDMs 1/2, over the current models, CDMs 3/4, or vice versa.

Acknowledgments

This work was supported by the Research Council of Norway (RCN) through the Center of Excellence "Autonomous Marine Operations and Systems" (NTNU AMOS), RCN project no. 223254.

The authors would like to thank the personnel from Kongsberg Maritime and the crew of R/V Gunnerus and for their help and support during the sea trials. A special thanks to Rune Skullestad and Øystein Lurås from Kongsberg Maritime for help with code implementation and the simulation platform to test the code. Also, the authors would like to thank the NTNU research team, Astrid H. Brodtkorb, Asgeir J. Sørensen, Mikkel E. N. Sørensen, Zhengru Ren, and Morten Breivik. Finally, MSc. Alexander Mykland deserves thanks for writing the test log. The authors would like to thank the anonymous reviewers for their constructive comments to improve the quality of this article.

Conflict of interest

None declared.

Appendix A. UKF-implementation

The implemented UKF is the discrete-time unscented Kalman Filter according to Simon (2006):

1. Discrete nonlinear system is given by

$$\boldsymbol{x}_{k+1} = \boldsymbol{f}(\boldsymbol{x}_k, \boldsymbol{u}_k, t_k) + \boldsymbol{\Gamma}(\boldsymbol{x}_k, t_k)\boldsymbol{w}_k \tag{17a}$$

$$\boldsymbol{y}_k = \boldsymbol{h}(\boldsymbol{x}_k, t_k) + \boldsymbol{v}_k \tag{17b}$$

$$\boldsymbol{w}_k \sim (0, \boldsymbol{Q}_k) \tag{17c}$$

$$\boldsymbol{v}_k \sim (0, \boldsymbol{R}_k), \tag{17d}$$

2. The UKF is initialized as

$$\hat{\boldsymbol{x}}_0^+ = E(\boldsymbol{x}_0) \tag{18a}$$

$$\boldsymbol{P}_0^+ = E[(\boldsymbol{x}_0 - \hat{\boldsymbol{x}}_0^+)(\boldsymbol{x}_0 - \hat{\boldsymbol{x}}_0^+)^\top] \tag{18b}$$

3. Time update equations:

$$\hat{\boldsymbol{x}}_{k-1} = \hat{\boldsymbol{x}}_{k-1}^+ + \tilde{\boldsymbol{x}}^{(i)}, \quad i = 1, \dots, 2n \tag{19a}$$

$$\tilde{\boldsymbol{x}}^{(i)} = \left(\sqrt{n\boldsymbol{P}_{k-1}^+}\right)_i^\top, \quad i = 1, \dots, n \tag{19b}$$

$$\tilde{\boldsymbol{x}}^{(n+i)} = -\left(\sqrt{n\boldsymbol{P}_{k-1}^+}\right)_i^\top, \quad i = 1, \dots, n \tag{19c}$$

$$\hat{\boldsymbol{x}}_k^{(i)} = \boldsymbol{f}(\hat{\boldsymbol{x}}_{k-1}^{(i)}, \boldsymbol{u}_k, t_k) \tag{19d}$$

$$\hat{\boldsymbol{x}}_k^- = \frac{1}{2n}\sum_{i=1}^{2n} \hat{\boldsymbol{x}}_k^{(i)} \tag{19e}$$

$$\boldsymbol{P}_k^- = \frac{1}{2n}\sum_{i=1}^{2n}\left(\hat{\boldsymbol{x}}_k^{(i)} - \hat{\boldsymbol{x}}_k^-\right)\left(\hat{\boldsymbol{x}}_k^{(i)} - \hat{\boldsymbol{x}}_k^-\right)^\top + \boldsymbol{\Gamma}(\boldsymbol{x}_k, t_k)\boldsymbol{Q}_{k-1}\boldsymbol{\Gamma}(\boldsymbol{x}_k, t_k)^\top \tag{19f}$$

Table 9
Mass and damping coefficients, control design model simulation verification model.

Coefficient	Value	Coefficient	Value
m_{11} [kg]	6 684 200	$Y_{\|v\|v}$ [$\frac{\text{kg}}{\text{m}}$]	−182 481
m_{22} [kg]	11 332 800	$Y_{\|r\|v}$ [$\frac{\text{kg}}{\text{rad}}$]	−1 922 557
m_{33} [$\frac{\text{kg m}^2}{\text{rad}}$]	3 193 127 000	$Y_{\|v\|r}$ [$\frac{\text{kg}}{\text{rad}}$]	−1 469 858
X_u [$\frac{\text{kg}}{\text{s}}$]	−167 105	$Y_{\|r\|r}$ [$\frac{\text{kg m}}{\text{rad}^2}$]	1 298 060
Y_v [$\frac{\text{kg}}{\text{s}}$]	−141 660	$N_{\|v\|v}$ [kg]	−702 742
Y_r [$\frac{\text{kg m}}{\text{rad s}}$]	650 440	$N_{\|r\|v}$ [$\frac{\text{kg m}}{\text{rad}}$]	2 383 317
N_v [$\frac{\text{kg m}}{\text{s}}$]	650 440	$N_{\|v\|r}$ [$\frac{\text{kg m}}{\text{rad}}$]	379 526
N_r [$\frac{\text{kg m}^2}{\text{rad s}}$]	−63 862 540	$N_{\|r\|r}$ [$\frac{\text{kg m}^2}{\text{rad}^2}$]	−10 683 000
$X_{\|u\|u}$ [$\frac{\text{kg}}{\text{m}}$]	−14 778	–	–

Table 10
Mass and damping coefficients, control design model R/V Gunnerus.

Coefficient	Value	Coefficient	Value
m_{11} [kg]	788 900	$Y_{\|v\|v}$ [$\frac{\text{kg}}{\text{m}}$]	−12 212
m_{22} [kg]	924 500	$Y_{\|r\|v}$ [$\frac{\text{kg}}{\text{rad}}$]	−131 673
m_{33} [$\frac{\text{kg m}^2}{\text{rad}}$]	51 240 000	$Y_{\|v\|r}$ [$\frac{\text{kg}}{\text{rad}}$]	2 224 318
X_u [$\frac{\text{kg}}{\text{s}}$]	−4949	$Y_{\|r\|r}$ [$\frac{\text{kg m}}{\text{rad}^2}$]	1 234 186
Y_v [$\frac{\text{kg}}{\text{s}}$]	−34 890	$N_{\|v\|v}$ [kg]	−163 526
Y_r [$\frac{\text{kg m}}{\text{rad s}}$]	−1 292 126	$N_{\|r\|v}$ [$\frac{\text{kg m}}{\text{rad}}$]	3 568 858
N_v [$\frac{\text{kg m}}{\text{s}}$]	−1 292 126	$N_{\|v\|r}$ [$\frac{\text{kg m}}{\text{rad}}$]	−6 564 338
N_r [$\frac{\text{kg m}^2}{\text{rad s}}$]	−66 285 641	$N_{\|r\|r}$ [$\frac{\text{kg m}^2}{\text{rad}^2}$]	0
$X_{\|u\|u}$ [$\frac{\text{kg}}{\text{m}}$]	−2275	–	–

4. Measurement update equations:

$$\hat{\boldsymbol{x}}_k = \hat{\boldsymbol{x}}_k^- + \tilde{\boldsymbol{x}}^{(i)}, \quad i = 1, \dots, 2n \tag{20a}$$

$$\tilde{\boldsymbol{x}}^{(i)} = \left(\sqrt{n\boldsymbol{P}_{k-1}^+}\right)_i^\top, \quad i = 1, \dots, n \tag{20b}$$

$$\tilde{\boldsymbol{x}}^{(n+i)} = -\left(\sqrt{n\boldsymbol{P}_{k-1}^+}\right)_i^\top, \quad i = 1, \dots, n \tag{20c}$$

$$\hat{\boldsymbol{y}}_k^{(i)} = \boldsymbol{h}(\hat{\boldsymbol{x}}_k^{(i)}, t_k) \tag{20d}$$

$$\hat{\boldsymbol{y}}_k = \frac{1}{2n}\sum_{i=1}^{2n} \hat{\boldsymbol{y}}_k^{(i)} \tag{20e}$$

$$\boldsymbol{P}_{\boldsymbol{y}} = \frac{1}{2n}\sum_{i=1}^{2n} \left(\hat{\boldsymbol{y}}_k^{(i)} - \hat{\boldsymbol{y}}_k\right)\left(\hat{\boldsymbol{y}}_k^{(i)} - \hat{\boldsymbol{y}}_k\right)^\top + \boldsymbol{R}_k \tag{20f}$$

$$\boldsymbol{P}_{\boldsymbol{xy}} = \frac{1}{2n}\sum_{i=1}^{2n} \left(\hat{\boldsymbol{x}}_k^{(i)} - \hat{\boldsymbol{x}}_k^-\right)\left(\hat{\boldsymbol{y}}_k^{(i)} - \hat{\boldsymbol{y}}_k\right)^\top \tag{20g}$$

$$\boldsymbol{K}_k = \boldsymbol{P}_{\boldsymbol{xy}}\boldsymbol{P}_{\boldsymbol{y}}^{-1} \tag{20h}$$

$$\hat{\boldsymbol{x}}_k^+ = \hat{\boldsymbol{x}}_k^- + \boldsymbol{K}_k(\boldsymbol{y}_k - \hat{\boldsymbol{y}}_k) \tag{20i}$$

$$\boldsymbol{P}_k^+ = \boldsymbol{P}_k^- - \boldsymbol{K}_k\boldsymbol{P}_{\boldsymbol{y}}\boldsymbol{K}_k^\top. \tag{20j}$$

Appendix B. Control design model for the simulation verification model

The simulation verification model is a 6 DOF model of a supply ship, and is part of the MCSim repository based on the MSS GNC toolbox (Fossen & Perez, 2004). For its corresponding 3 DOF control design model, the linear damping and mass matrix are known from the simulation model, whereas the nonlinear damping matrix is identified as discussed in Section 4. The matrices are given below and the parameter values are given in Table 9.

$$\boldsymbol{M} = \text{diag}\{m_{11}, m_{22}, m_{33}\} \tag{21}$$

$$\boldsymbol{D}_L = \begin{bmatrix} -X_u & 0 & 0 \\ 0 & -Y_v & -Y_r \\ 0 & -N_v & -N_r \end{bmatrix} \tag{22}$$

$$\boldsymbol{D}_{NL}(\nu_r) = \begin{bmatrix} d_{11} & 0 & 0 \\ 0 & d_{22} & d_{23} \\ 0 & d_{32} & d_{33} \end{bmatrix}, \tag{23}$$

where $d_{11} = -X_{|u|u}|u_r|$, $d_{22} = -Y_{|v|v}|v_r| - Y_{|r|v}|r|$, $d_{23} = -Y_{|v|r}|v_r| - Y_{|r|r}|r|$, $d_{32} = -N_{|v|v}|v_r| - N_{|r|v}|r|$, $d_{33} = -N_{|v|r}|v_r| - N_{|r|r}|r|$.

Appendix C. R/V Gunnerus control design model

For the NTNU-owned vessel R/V Gunnerus, observers are tested on real data captured during DP operations at the AMOS DP Research Cruise 2016 (Skjetne et al., 2017). In the observers, the mass matrix applied has been calculated using ShipX VeRes (MARINTEK, 0000), whereas the damping matrices are identified as discussed in Section 4. The matrices are given below and the parameter values are given in Table 10.

$$\boldsymbol{M} = \text{diag}\{m_{11}, m_{22}, m_{33}\} \tag{24}$$

$$\boldsymbol{D}_L = \begin{bmatrix} -X_u & 0 & 0 \\ 0 & -Y_v & -Y_r \\ 0 & -N_v & -N_r \end{bmatrix} \tag{25}$$

$$\boldsymbol{D}_{NL}(\nu_r) = \begin{bmatrix} d_{11} & 0 & 0 \\ 0 & d_{22} & d_{23} \\ 0 & d_{32} & d_{33} \end{bmatrix}, \tag{26}$$

where $d_{11} = -X_{|u|u}|u_r|$, $d_{22} = -Y_{|v|v}|v_r| - Y_{|r|v}|r|$, $d_{23} = -Y_{|v|r}|v_r| - Y_{|r|r}|r|$, $d_{32} = -N_{|v|v}|v_r| - N_{|r|v}|r|$, $d_{33} = -N_{|v|r}|v_r| - N_{|r|r}|r|$.

$N_{|r|r}$ is zero because the identification results provided slightly negative and slightly positive values for the coefficient (for different data series). Therefore, it was set to zero.

References

Balchen, J. G., Jenssen, N. A., & Sælid, S. (1976). Dynamic positioning using Kalman filtering and optimal control theory. In *IFAC/IFIP symposium on automation in offshore oil field operation, Vol. 183* (p. 186).

Candeloro, M., Sørensen, A. J., Longhi, S., & Dukan, F. (2012). Observers for dynamic positioning of ROVs with experimental results. In *Proceedings of the IFAC conference on manoeuvring and control of marine craft 2012, Vol. 45(27)* (pp. 85–90).

Chen, C. -T. (2009). *Linear system theory and design* (3rd ed.). Oxford University Press, Inc..

Fossen, T. I. (2011). *Handbook of marine craft hydrodynamics and motion control*. John Wiley & Sons.

Fossen, T. I., & Perez, T. (2004). Marine Systems Simulator (MSS), https://github.com/cybergalactic/MSS Accessed: 2017-02-24.

Fossen, T. I., & Perez, T. (2009). Kalman filtering for positioning and heading control of ships and offshore rigs. *IEEE Control Systems*, *29*(6), 32–46.

Fossen, T. I., & Strand, J. P. (1999). Passive nonlinear observer design for ships using Lyapunov methods: full-scale experiments with a supply vessel. *Automatica*, *35*(1), 3–16.

Fung, P., & Grimble, M. (1983). Dynamic ship positioning using a self-tuning Kalman filter. *IEEE Transactions on Automatic Control*, *28*(3), 339–350.

Grimble, M. J., Patton, R., & Wise, D. (1980). Use of kalman filtering techniques in dynamic ship-positioning systems. In *IEE proceedings D-control theory and applications, Vol. 127* (p. 93). IET.

Hassani, V., Pascoal, A. M., Aguiar, A. P., et al. (2012). Multiple model adaptive wave filtering for dynamic positioning of marine vessels. In *American control conference (ACC), Vol. 2012* (pp. 6222–6228). IEEE.

Kjerstad, Ø. K., & Skjetne, R. (2016). Disturbance rejection by acceleration feedforward for marine surface vessels. *IEEE Access*, *4*, 2656–2669.

Loria, A., Fossen, T. I., & Panteley, E. (2000). A separation principle for dynamic positioning of ships: Theoretical and experimental results. *IEEE Transactions on Control Systems Technology*, *8*(2), 332–343.

MARINTEK (n.d.) ShipX VeRes, https://www.sintef.no/en/software/shipx/ Accessed: 2018-04-18.

Price, W. G., & Bishop, R. E. D. (1974). *Probabilistic theory of ship dynamics*. Halsted Press.

Refsnes, J. E. G. (2007). *Nonlinear model-based control of slender body AUVs* (PhD thesis), Norwegian University of Science and Technology, Trondheim, Norway.

Refsnes, J. E., & Sørensen, A. J. (2007). Comparison of two observers for marine vessels in ocean current. In *Proceedings of the IFAC conference on control applications in marine systems 2007, Vol. 40(17)* (pp. 32–37). Elsevier.

Saelid, S., Jenssen, N., & Balchen, J. (1983). Design and analysis of a dynamic positioning system based on Kalman filtering and optimal control. *IEEE Transactions on Automatic Control*, *28*(3), 331–339.

Simon, D. (2006). *Optimal state estimation: Kalman, H infinity, and nonlinear approaches*. John Wiley & Sons.

Skjetne, R., Sørensen, M. E. N., Breivik, M., Værnø, S. A., Brodtkorb, A. H., & Sørensen, A. J. (2017). AMOS DP Research cruise 2016: Academic full-scale testing of experimental dynamic positioning control algorithms onboard R/V Gunner us. In *ASME 2017 36th international conference on ocean, offshore and arctic engineering*. American Society of Mechanical Engineers.

Sørensen, A. J. (2011). A survey of dynamic positioning control systems. *Annual Reviews Control*, *35*(1), 123–136.

Sørensen, A. J. (2013). *Marine control systems - lecture notes*. Department of Marine Technology, Norwegian Univ. of Sci. and Tech..

Tannuri, E., & Morishita, H. (2006). Experimental and numerical evaluation of a typical dynamic positioning system. *Applied Ocean Research*, *28*(2), 133–146.

Veritas, D. N. (2011). Dynamic Positioning Systems-Operation Guidance.